

A universal 21 cm signature of growing massive black holes in the early Universe

S. Sazonov^{1,2*} and I. Khabibullin^{3,1}

¹*Space Research Institute, Russian Academy of Sciences, Profsoyuznaya 84/32, 117997 Moscow, Russia*

²*National Research University Higher School of Economics, Myasnitskaya ul. 20, 101000 Moscow, Russia*

³*Max Planck Institute for Astrophysics, Karl-Schwarzschild-Strasse 1, D-85741 Garching, Germany*

8 August 2019

ABSTRACT

There is a hope that looking into the early Universe with next-generation telescopes, one will be able to observe the early accretion growth of supermassive black holes (BHs) when their masses were $\sim 10^4\text{--}10^6 M_\odot$. According to the standard accretion theory, the bulk of the gravitational potential energy released by radiatively efficient accretion of matter onto a BH in this mass range is expected to be emitted in the extreme UV–ultrasoft X-ray bands. We demonstrate that such a ‘miniquasar’ at $z \sim 15$ should leave a specific, localized imprint on the 21 cm cosmological signal. Namely, its position on the sky will be surrounded by a region with a fairly sharp boundary of several arcmin radius, within which the 21 cm brightness temperature quickly grows inwards from the background value of ~ -250 mK to $\sim +30$ mK. The size of this region is only weakly sensitive to the BH mass, so that the flux density of the excess 21 cm signal is expected to be $\sim 0.1\text{--}0.2$ mJy at $z \sim 15$ and should be detectable by the Square Kilometer Array. We argue that an optimal strategy would be to search for such signals from high- z miniquasar candidates that can be found and localized with a next-generation X-ray mission such as *Lynx*. A detection of the predicted 21 cm signal would provide a measurement of the growing BH’s redshift to within $\Delta z/(1+z) \lesssim 0.01$.

Key words: stars: black holes – accretion, accretion discs – galaxies: high-redshift – dark ages, reionization, first stars – quasars: supermassive black holes

1 INTRODUCTION

The discovery of powerful quasars at $z \approx 7.5$ (Bañados et al. 2018) implies that fully fledged supermassive black holes (BHs) as heavy as $M_{\text{BH}} \sim 10^9 M_\odot$ already existed when the Universe was just 700 million years old. If a significant fraction of this mass has been accumulated by accretion at a nearly critical rate, then the growth of such objects must have started very early on (at $z \gtrsim 20$) from seeds that already had masses $\sim 10^3 M_\odot$ or more. What kind of object these seeds were is one of the most interesting open questions in astrophysics (see Volonteri 2010; Latif & Ferrara 2016; Woods et al. 2018 for reviews). There is a hope that looking into the $z \sim 20\text{--}10$ epochs with next-generation telescopes, one will be able to observe the early accretion growth of supermassive BHs when their masses were $\sim 10^4\text{--}10^6 M_\odot$. Hereafter, we will refer to such accretors as ‘miniquasars’.

One of the most promising ways to find such miniquasars is in X-rays, since we know that both stellar-mass

and supermassive black holes emit copious amounts of X-rays during accretion (X-ray binaries, XRBs, and active galactic nuclei, AGN, respectively). Unfortunately, even the sensitivity of the *Chandra* X-ray Observatory is not sufficient for detecting miniquasars at $z \gtrsim 6$. The situation will change dramatically if a mission such as the proposed *Lynx* is implemented in the future. *Lynx* is planned to achieve a sensitivity as high as 10^{-19} erg cm⁻² s⁻¹ (0.5–2 keV) in combination with *Chandra*-like (arcsecond) angular resolution and substantial sky coverage (~ 400 arcmin²) in its deep extragalactic surveys (The *Lynx* Team 2018; Ben-Ami, Vikhlinin, & Loeb 2018). This implies that X-ray sources with luminosities as low as a few 10^{41} erg s⁻¹ (rest-frame 2–10 keV) will be detectable without confusion at $z \sim 15$. Assuming that hard X-ray emission carries a significant ($\sim 10\%$) fraction of the near-Eddington bolometric luminosity of a miniquasar, *Lynx* will be able to detect accreting BHs with masses as low as a few $10^4 M_\odot$ in the early Universe.

The bulk of the gravitational potential energy released during radiatively efficient accretion onto a BH emerges in the form of quasi-thermal radiation from the accretion disk

* E-mail: sazonov@iki.rssi.ru

(Shakura & Sunyaev 1973), with the effective waveband shifting from the optical–UV for supermassive BHs to soft X-rays for stellar-mass BHs, as observed in AGN and XRBs (in so-called soft/high states for the latter, e.g. Gilfanov & Merloni 2014). For intermediate-mass BHs, the bulk of the disk’s emission is expected to fall into the far UV–ultrasoft X-ray band. Therefore, due to cosmological redshift, *Lynx* will not be able to detect this primary emission component, but, as already mentioned above, it should be able to observe additional, harder radiation that can arise due to Comptonization of thermal emission from the disk in its hot corona. In principle, the redshifted thermal emission from miniquasars could be observed directly in the optical–infrared band, but since the Eddington luminosity for a BH of mass $\sim 10^5 M_\odot$ at $z \sim 15$ corresponds to an AB magnitude of more than 30, the detection of such miniquasars will be extremely challenging even with the next-generation IR observatories such as the *James Web Space Telescope* and *Wide-field Infrared Survey Telescope* (see Mason, Trenti, & Treu 2015 for the expected sensitivities of future surveys with these telescopes).

There is, however, another, indirect way to reveal the primary thermal radiation from the first miniquasars, which is to observe its impact on the ambient intergalactic medium (IGM) in the early Universe using the 21 cm spin-flip transition of neutral hydrogen. As has been actively discussed over the past two decades, the first generations of X-ray sources could significantly heat the primordial IGM prior to cosmic reionization and strongly modify the global 21 cm signal from the $z \sim 15$ – 10 epochs (see Pritchard & Loeb 2012 for a review). A lot of recent literature on this subject is devoted to discussing the potentially observable effect of the first generations of stellar-type X-ray sources and in particular high-mass X-ray binaries (HMXBs, e.g. Mirabel et al. 2011; Cohen et al. 2017; Madau & Fragos 2017; Sazonov & Khabibullin 2017a), which likely were present in significant numbers since the beginning of active star formation in the Universe (Fragos et al. 2013). The bulk of the emission produced by HMXBs is at energies above 0.5 keV and since such photons can travel large distances before being photoabsorbed in the IGM, the main effect of HMXBs is expected to be a global enhancement of the IGM temperature together with large-scale fluctuations reflecting the large-scale structure of the early Universe (e.g. Pritchard & Furlanetto 2007; Ross et al. 2017).

In contrast, miniquasars, which presumably have much softer energy spectra compared to HMXBs, should mainly heat the IGM in their relatively close vicinity. One may thus expect such sources to be surrounded by compact regions of specific 21 cm signal. Although finding such 21 cm features in a blind search might be difficult even for the most ambitious upcoming radio interferometers such as the Square Kilometer Array (SKA, Mellema et al. 2013), such a search could be greatly facilitated if carried out around miniquasar candidates found via their coronal X-ray emission with a mission like *Lynx*. We elaborate on this idea below. Before proceeding, we note that there have been plenty of studies addressing the impact of quasars and miniquasars on the IGM and the associated 21 cm signal (e.g. Madau et al. 2004; Ricotti & Ostriker 2004; Chuzhoy, Alvarez, & Shapiro 2006; Thomas & Zaroubi 2008; Yajima & Li 2014; Fialkov et al. 2017; Ghara et al. 2017; Bolgar et al. 2018; Vasiliev, Sethi, & Shchekinov 2018), but the novelty of our study is its focus

on the miniquasar’s primary, thermal emission component and the synergy of 21 cm and X-ray observations.

The following values of cosmological parameters are used throughout the paper: $\Omega_m = 0.309$, $\Omega_\Lambda = 1 - \Omega_m$, $\Omega_b = 0.049$, $H_0 = 68 \text{ km s}^{-1} \text{ Mpc}^{-1}$ and $Y = 0.246$ (helium mass fraction) (Planck Collaboration et al. 2016).

2 MODEL

Suppose a BH has an initial mass M_i at redshift z_i and accretes matter until epoch z_f , reaching a final mass M_f . If the accretion proceeded at a critical (Eddington limited) rate \dot{M}_E , the BH mass would be increasing exponentially,

$$M(t) = M_i e^{\frac{t}{t_S}}, \quad (1)$$

on the Salpeter time scale $t_S = \frac{\epsilon}{1-\epsilon} \frac{c^2 M_\odot}{L_{\text{Edd}}(M_\odot)}$, where L_{Edd} is the Eddington luminosity and ϵ is the radiation efficiency. Adopting for simplicity $\epsilon = 0.1$ (as is approximately true for standard accretion disks), $t_S \approx 5 \times 10^7 \text{ yr}$. Therefore, the average rate expressed in units of the critical rate (usually referred to as the Eddington ratio), at which the BH accretes mass between epochs z_i and z_f is

$$\langle \dot{m} \rangle \equiv \frac{\dot{M}}{\dot{M}_E} = \frac{t_S}{t(z_i, z_f)} \ln \frac{M_f}{M_i}, \quad (2)$$

where $t(z_i, z_f)$ is the cosmic time between z_i and z_f .

It is unlikely though that the BH will accrete matter at a constant rate over a cosmologically long period of time. In reality, accretion onto the BH will be determined by evolving external and internal (with respect to the host galaxy) conditions and is likely to be an intermittent process. Therefore, in our simulations, described below, we assumed that there are periods of active accretion when the Eddington ratio takes a fixed value \dot{m} and passive periods when $\dot{m} = 0$. We further assume that these two types of intervals alternate in a random fashion¹, so that the duty cycle of BH activity is

$$k_{\text{duty}} = \frac{\langle \dot{m} \rangle}{\dot{m}}. \quad (3)$$

By definition, $\dot{m} \geq \langle \dot{m} \rangle$, and we also assume that $\dot{m} < 1$, i.e. we do not consider supercritical accretion in this study.

2.1 Emission spectrum

One of the key aspects for this study is the spectrum of the radiation emitted by the accreting BH. According to the standard accretion theory (Shakura & Sunyaev 1973), a geometrically thin, optically thick accretion disk around a BH is characterized by a $\propto r^{-3/4}$ temperature profile (except in the very narrow innermost region, where only a small fraction of the total luminosity is emitted) and generates multi-color, nearly blackbody radiation with a spectrum (specific luminosity as a function of energy)

$$L_E(E) \propto \int_{r_{\text{in}}}^{r_{\text{out}}} r B_E(E, T(r)) dr, \quad (4)$$

where r_{in} and r_{out} are the disk’s inner and outer radii and B_E is the Planck function.

¹ We took the duration of these intervals to be $\Delta t = 10^4$ or 10^5 yr , with the results being insensitive to this choice as long as $\Delta t \ll t_S$.

The maximum temperature of the disk is

$$kT_{\max} \approx 1.2 \left(\frac{\dot{m}}{m} \right)^{1/4} \text{ keV}, \quad (5)$$

where $m(t)$ is the growing BH mass expressed in solar masses. According to the standard theory, this temperature is achieved at $(49/36)r_0$, where r_0 is the radius of the innermost stable circular orbit, but a fairly good approximation is that the disk temperature reaches this value at r_{in} and then decreases as $T(r) = T_{\max}(r/r_{\text{in}})^{-3/4}$ at $r > r_{\text{in}}$. For the purposes of this study it can also be safely assumed that $r_{\text{out}} \rightarrow \infty$. The spectrum given by equation (4) can then be approximated by the power law $L_E \propto E^{1/3}$ at $E \lesssim 0.3kT_{\max}$ and by the blackbody spectrum with a temperature of $0.7T_{\max}$ at $E \gtrsim 2kT_{\max}$ (Makishima et al. 1986), with its maximum (when plotted in units of EL_E) being at $E_{\max} \approx 2.35kT_{\max}$. The normalization constant in equation (4) is determined by the condition

$$\int L_E dE = \dot{m}L_{\text{Edd}}(m). \quad (6)$$

The model described above is widely known as a multicolor disk blackbody model (*diskbb* in XSPEC, Arnaud 1996), and we have chosen it as our baseline spectral model. This choice is primarily motivated by the fact that the standard accretion disk theory provides a satisfactory description of the observed spectral energy distributions (SED) of (i) XRBs in their soft/high states (when $\dot{m} \gtrsim 0.1$); namely, their dominant emission component is well described by *diskbb* with $kT_{\max} \lesssim 1$ keV, as expected from equation (5) for the stellar masses ($m \lesssim 10$) of the BHs in XRBs (see Done, Gierliński, & Kubota 2007 for a review) and (ii) AGN – supermassive BHs accreting at $\dot{m} \sim 0.01$ –1, for which the peak of the SED is observed in the optical-UV (the so-called big blue bump, e.g. Elvis et al. 1994; Telfer et al. 2002; Sazonov, Ostriker, & Sunyaev 2004), again as expected from equation (5) for the high ($m \sim 10^7$ – 10^9) BH masses of AGN.

In reality, observations reveal significant deviations of XRB and AGN spectra from the simple multicolor disk blackbody model described above, and these deviations can be generally accounted for by the conditions at the inner boundary of the accretion disk, radiative transfer effects in the disk’s atmosphere and relativistic corrections (e.g. Koratkar & Blaes 1999; Merloni, Fabian, & Ross 2000; Davis et al. 2005; Done et al. 2012). However, in view of other, larger uncertainties related to the problem in hand (in particular in the BH mass and accretion rate), we do not take these subtleties into account.

Arguing further from analogy with XRBs and AGNs, it is likely that a miniquasar’s emission spectrum has an additional, harder component due to the Comptonization of part of the thermal radiation from the disk in its hot corona. We simulate this plausible situation by modifying our baseline *diskbb* model by the *simpl* (Steiner et al. 2009) model [specifically we use *simpl(diskbb)* in XSPEC], which provides a simplified description of Comptonization by converting a given fraction, f_{sc} , of soft thermal photons into high-energy ones. Another free parameter of this model is the photon index, Γ , of the power-law component. We use $\Gamma = 2$ and $f_{\text{sc}} = 0.05$ as fiducial values. The assumed spectral slope is close to those of observed hard X-ray tails in XRBs and AGN and is convenient in use since no k -correction is then needed in converting luminosities to fluxes. The adopted f_{sc}

value implies that the power-law component, if it continues up to $E \sim 100$ keV, contains $\sim 25\%$ (with a very weak dependence on the disk temperature, i.e. on m and \dot{m}) of the miniquasar’s bolometric luminosity, in overall agreement with observations of XRBs in their high state (e.g. Done, Gierliński, & Kubota 2007) and AGN (e.g. Sazonov, Ostriker, & Sunyaev 2004). Note that for the adopted values of the parameters, Γ may be considered the slope of the high-energy part of the spectrum at $E \gtrsim 10kT_{\max}$, where T_{\max} is given by equation (5).

As already mentioned, our current treatment is restricted to the case of subcritical accretion ($\dot{m} < 1$). In reality, in some miniquasars and/or at some stage of their evolution accretion may proceed at a supercritical rate. Consideration of such a case would require adopting a substantially different spectral model, as suggested by the measured spectra of individual ultraluminous X-ray sources in nearby galaxies (e.g. Sazonov, Lutovinov, & Krivonos 2014; Kaaret, Feng & Roberts 2017), the collective X-ray spectrum of such sources in the local Universe (Sazonov & Khabibullin 2017b) and theoretical considerations (e.g. Narayan, Sałdowski & Soria 2017; Takeo et al. 2019).

2.2 Intragalactic absorption

Before reaching the ambient IGM, the extreme UV-soft X-ray radiation from the miniquasar may be partially photoabsorbed within its host galaxy. This may happen (i) in the vicinity of the BH if something like the AGN obscuring torus is present in miniquasars (in that case, absorption will take place within a certain solid angle only), and/or (ii) in the more distant regions of the galaxy. Given our scarce knowledge about the first galaxies and in particular about the parsec-scale environment of intermediate-mass BHs they may host, and also taking into account that the miniquasar’s radiation can significantly ionize the interstellar medium in front of it and thereby strongly diminish the net absorption effect (see, e.g., Sazonov & Khabibullin 2018), it is hardly possible to reliably predict the typical line-of-sight absorption column, N_{H} , for the miniquasars in the early Universe. We therefore consider it a free parameter. Similarly, we allow the metallicity of the absorbing gas to vary from $Z = 0$ (pure H–He gas) to $Z = 1$ (normal chemical composition): although the first galaxies (at $z \sim 20$ –10) were likely metal poor, the immediate surroundings of miniquasars might have been significantly metal enriched because they were probably the sites of strong star formation activity.

Figure 1 (top panel) shows examples of (rest-frame) spectra of miniquasars for various values of model parameters, namely m (assuming $\dot{m} = 1$), N_{H} and Z (absorption was modeled by means of the *tbvarabs* model in XSPEC). We see that for the range of BH masses and accretion rates expected for miniquasars and in the absence of absorption, the bulk of the accretion disk’s emission is in the extreme UV–very soft X-ray band, at energies $E \sim 50$ –1000 eV. Even a moderate absorption ($N_{\text{H}} \lesssim 10^{20} \text{ cm}^{-2}$) will cause a strong reduction of the flux below ~ 200 eV. An addition of metals to the absorbing medium (the $Z = 1$ case) will further reduce the flux, but mostly above the oxygen absorption edge at $E = 536$ eV (note also that the helium absorption edge at $E = 24.6$ eV is clearly seen in the spectra).

The bottom panel of Fig. 1 shows examples of thermal

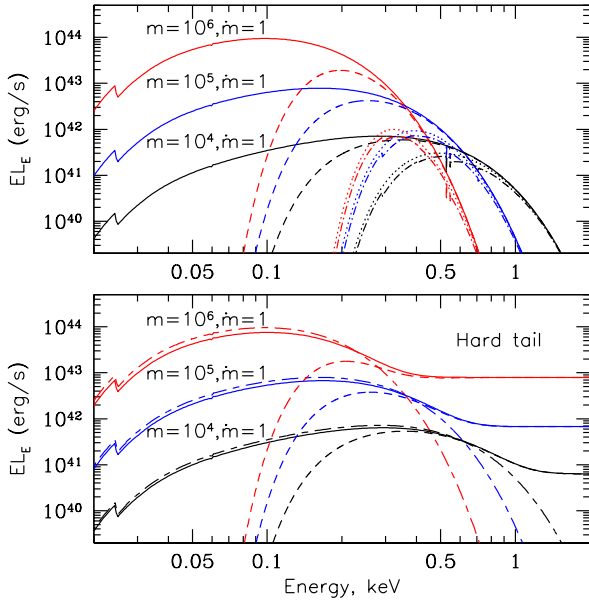


Figure 1. *Top panel:* Multicolor disk blackbody emission spectra (in the source’s rest frame, in units of specific luminosity multiplied by photon energy) modified by absorption in the miniquasar’s host galaxy, for $\dot{m} = 1$, different BH masses, $m = 10^4$ (black), 10^5 (blue) and 10^6 (red), and various absorption columns and metallicities (N_{H} in cm^{-2} , Z): $(10^{18}, 0)$ – solid, $(10^{20}, 0)$ – dashed, $(10^{21}, 0)$ – dotted, $(10^{21}, 1)$ – dash-dotted. *Bottom panel:* Multicolor disk blackbody emission spectra modified by Comptonization (*simpl(diskbb)*), for the same BH masses as above (shown with the same colors). The solid and dashed curves correspond to $N_{\text{H}} = 10^{18} \text{ cm}^{-2}$ and $N_{\text{H}} = 10^{20} \text{ cm}^{-2}$, respectively ($Z = 0$). The corresponding pure thermal spectra (for $N_{\text{H}} = 10^{18} \text{ cm}^{-2}$) are shown with the short dash–long dashed lines for comparison.

spectra modified by Comptonization, as described above. For the adopted value, $f_{\text{sc}} = 0.05$, of the fraction of Comptonized photons, the hard tail starts to dominate over thermal emission at $\sim 1 \text{ keV}$ for the lowest mass BH ($m = 10^4$) and already at $\sim 300 \text{ eV}$ for the highest mass BH ($m = 10^6$).

3 A CRUDE ESTIMATE OF THE EXPECTED HEATING

To a first approximation, the thermal disk emission from miniquasars (with $m \sim 10^4\text{--}10^6$) in the presence of moderate absorption ($N_{\text{H}} \lesssim 10^{20} \text{ cm}^{-2}$) may be characterized by a narrow spectrum around an energy $\sim 300 \text{ eV}$ (see Fig. 1). This allows us to derive order-of-magnitude estimates for the impact of a miniquasar on the IGM before proceeding to detailed computations.

The mean free path of soft X-ray photons of energy E in the primordial (i.e. nearly neutral H–He gas) IGM of the early Universe can be approximated as follows (Sazonov & Sunyaev 2015):

$$\bar{\lambda} \approx 740 \left(\frac{1+z}{11} \right)^{-3} \left(\frac{E}{300 \text{ eV}} \right)^{3.2} \text{ kpc}. \quad (7)$$

Within this (proper) distance from the source, $1 - e^{-1} \approx 63\%$

of photons of energy E will be photoabsorbed (whereas 95% of photons will be absorbed within $3\bar{\lambda}$). The distance $\bar{\lambda}$ corresponds to an angular size

$$\bar{\theta} \approx 2.7 \left(\frac{1+z}{11} \right)^{-2} \left(\frac{E}{300 \text{ eV}} \right)^{3.2} \text{ arcmin}, \quad (8)$$

on the sky, which is a reasonably good approximation for $z = 20\text{--}10$ and $E = 100\text{--}1000 \text{ eV}$.

The thermal disk emission from a miniquasar can heat the IGM efficiently only within a few $\bar{\lambda}$, since only an exponentially decreasing fraction of the miniquasar’s luminosity reaches larger distances. This allows us to readily estimate the expected IGM temperature increment. The total energy released by the BH during its growth to mass M is $W = \epsilon M c^2$, and we may assume that most of this energy is radiated away over a time of order the Salpeter time (t_{S}) just before the epoch when the miniquasar and the associated 21 cm signal are observed, so that, to a first approximation, we can ignore any effects associated with the expansion of the Universe. We may further assume that all of this energy has been absorbed within a volume of radius $\sim \bar{\lambda}$ (the corresponding light travel time proves to be shorter than t_{S}). Assuming that the miniquasar ionizes the surrounding medium only moderately (i.e. the ionization degree of hydrogen is less than a few per cent, which is a good approximation for the bulk of the affected volume), we may roughly estimate the mean fraction of the energy of soft X-ray photons that goes into heating the IGM as $f_{\text{heat}} \sim 0.2$ (Furlanetto & Stoever 2010). Taking into account that the hydrogen space density changes with redshift as $n_{\text{H}}(z) \approx 2.6 \times 10^{-4} [(1+z)/11]^3 \text{ cm}^{-3}$, we can write

$$f_{\text{heat}} W = \frac{4\pi \bar{\lambda}^3}{3} \frac{3}{2} n_{\text{H}} k \Delta T_{\text{K}}, \quad (9)$$

where k is the Boltzmann constant, and finally determine the expected IGM temperature increment assuming $E = 300 \text{ eV}$:

$$\Delta T_{\text{K}} \sim 100 \frac{f_{\text{heat}}}{0.2} \frac{\epsilon}{0.1} \left(\frac{1+z}{11} \right)^6 \frac{m}{10^4} \text{ K}. \quad (10)$$

Comparing this with the cosmic microwave background (CMB) temperature, $T_{\text{CMB}}(z) \approx 30[(1+z)/11]$, we come to the conclusion that BHs with $M \gtrsim 10^4 M_{\odot}$ accreting at a nearly critical rate in the early Universe will be surrounded by well-defined zones with a radius of a few arcmin within which $T_{\text{K}} \gtrsim T_{\text{CMB}}$, and these regions are thus expected to be 21 cm emitters, in contrast to the surrounding sky, which is likely to exhibit 21 cm absorption at $z \gtrsim 10$. Importantly, for $m \gtrsim 10^4$, the size of the heating region is determined simply by the mean free path of soft X-ray photons, rather than by the radiative power of the miniquasar. Following the same argument, we may expect that for BHs of smaller mass, $m \lesssim 10^4$, the region of strong heating [$\Delta T_{\text{K}} \gtrsim T_{\text{CMB}}(z)$] will be smaller than $\sim \bar{\lambda}$ and its actual size will be determined by the total energy released by accretion onto the BH.

4 SIMULATIONS

Based on the assumptions outlined in §2, we performed a series of numerical calculations of IGM heating and associated 21 cm emission/absorption in the vicinity of miniquasars in the early Universe. We limited simulations to a redshift

range of $z = 20$ – 10 and neglected any global heating (i.e. outside the region affected by the miniquasar) of the IGM by X-ray sources and/or other mechanisms². We adopted the following initial parameters of the IGM: $x_{\text{HII}} \equiv n_{\text{HII}}/n_{\text{H}} = 2.2 \times 10^{-4}$ (hydrogen ionization fraction), $x_{\text{HeII}} \equiv n_{\text{HeII}}/n_{\text{He}} = 0$, $x_{\text{HeIII}} \equiv n_{\text{HeIII}}/n_{\text{He}} = 0$ (helium ionization fractions) and either $T_{\text{K}} = 9.3$ K (for $z_i = 20$) or $T_{\text{K}} = 5.4$ K (for $z_i = 15$). These were found using RECFAST (Seager, Sasselov, & Scott 1999) and correspond to the conditions after cosmic recombination and adiabatic cooling of the primordial gas. Our assumption about the absence of significant global heating might be a good approximation at least at $z \gtrsim 15$, as suggested by the recent detection of a strong, sky-averaged 21 cm absorption signal in the Experiment to Detect the Global Epoch of Reionization Signature (EDGES, Bowman et al. 2018).

X-ray ionization and heating of the IGM was calculated in logarithmically binned spherical shells around the miniquasar, out to a comoving distance of 500 Mpc. Although this maximal distance is fairly large, we ignored photon travel time effects (i.e. the response of the IGM to radiation emitted by the central source was considered instantaneous), since X-ray heating proves to be noticeable only within ~ 30 cMpc of the miniquasar and the corresponding light travel time at $z \gtrsim 10$ is much shorter than the Salpeter timescale on which BH growth occurs.

The evolution of the ionization state of hydrogen and helium with time in a given shell was calculated as follows [equations (11)–(15) below are adopted from Madau & Fragos 2017; Sazonov & Khabibullin 2017a]:

$$\begin{aligned} \frac{dx_{\text{HI}}}{dt} &= -x_{\text{HI}}\Gamma_{\text{HI}} + n_e(1 - x_{\text{HI}})\alpha_{\text{HII}}, \\ \frac{dx_{\text{HeI}}}{dt} &= -x_{\text{HeI}}\Gamma_{\text{HeI}} + n_e x_{\text{HeII}}\alpha_{\text{HeII}}, \\ \frac{dx_{\text{HeII}}}{dt} &= -x_{\text{HeII}}\Gamma_{\text{HeII}} + n_e x_{\text{HeIII}}\alpha_{\text{HeIII}} - \frac{dx_{\text{HeI}}}{dt}, \end{aligned} \quad (11)$$

where n_e is the number density of free electrons, α_{HII} , α_{HeII} and α_{HeIII} are the recombination coefficients (adopted from Theuns et al. 1998), and Γ_{HI} , Γ_{HeI} and Γ_{HeII} are the photoionization coefficients, which were calculated as follows:

$$\begin{aligned} \Gamma_{\text{HI}} &= \frac{1}{4\pi r^2} \left(\int_{I_{\text{HI}}}^{\infty} \frac{L_E e^{-\tau(r,E)}}{E} \sigma_{\text{HI}} (1 + N_{\text{s,HI}}(E, I_{\text{HI}})) dE \right. \\ &\quad + \int_{I_{\text{HeI}}}^{\infty} \frac{L_E e^{-\tau(r,E)}}{E} \sigma_{\text{HeI}} \frac{n_{\text{HeI}}}{n_{\text{HI}}} N_{\text{s,HI}}(E, I_{\text{HeI}}) dE \\ &\quad \left. + \int_{I_{\text{HeII}}}^{\infty} \frac{L_E e^{-\tau(r,E)}}{E} \sigma_{\text{HeII}} \frac{n_{\text{HeII}}}{n_{\text{HI}}} N_{\text{s,HI}}(E, I_{\text{HeII}}) dE \right), \\ \Gamma_{\text{HeI}} &= \frac{1}{4\pi r^2} \left(\int_{I_{\text{HI}}}^{\infty} \frac{L_E e^{-\tau(r,E)}}{E} \sigma_{\text{HI}} \frac{n_{\text{HI}}}{n_{\text{HeI}}} N_{\text{s,HeI}}(E, I_{\text{HI}}) dE \right. \\ &\quad + \int_{I_{\text{HeI}}}^{\infty} \frac{L_E e^{-\tau(r,E)}}{E} \sigma_{\text{HeI}} (1 + N_{\text{s,HeI}}(E, I_{\text{HeI}})) dE \\ &\quad \left. + \int_{I_{\text{HeII}}}^{\infty} \frac{L_E e^{-\tau(r,E)}}{E} \sigma_{\text{HeII}} \frac{n_{\text{HeII}}}{n_{\text{HeI}}} N_{\text{s,HeI}}(E, I_{\text{HeII}}) dE \right), \\ \Gamma_{\text{HeII}} &= \frac{1}{4\pi r^2} \int_{I_{\text{HeII}}}^{\infty} \frac{L_E e^{-\tau(r,E)}}{E} \sigma_{\text{HeII}} dE, \end{aligned} \quad (12)$$

² In particular, by low-energy cosmic rays from the first super-novae (Sazonov & Sunyaev 2015; Leite et al. 2017).

where $I_{\text{HI}} = 13.6$ eV, $I_{\text{HeI}} = 24.6$ eV and $I_{\text{HeII}} = 54.4$ eV are the ionization thresholds for HI, HeI and HeII, $N_{\text{s,HI}}$ and $N_{\text{s,HeI}}$ are the mean numbers of secondary ionizations of HI and HeI (secondary ionization of HeII is practically unimportant) caused by the fast photoelectron, with the notation $N_{\text{s,HI}}(E, I_{\text{HI}})$ meaning that $N_{\text{s,HI}}$ is a function of the photoelectron energy, $E - I_{\text{HI}}$ (the corresponding dependencies for HI and HeI are adopted from Furlanetto & Stoever 2010), and

$$\tau(r, E) = \int_0^r [n_{\text{HI}}(r')\sigma_{\text{HI}}(E) + n_{\text{HeI}}(r')\sigma_{\text{HeI}}(E) + n_{\text{HeII}}(r')\sigma_{\text{HeII}}(E)] dr' \quad (13)$$

is the IGM photoionization optical depth within radius r from the source, with the cross-sections $\sigma_{\text{HI}}(E)$, $\sigma_{\text{HeI}}(E)$ and $\sigma_{\text{HeII}}(E)$ adopted from Verner et al. (1996).

The evolution of the gas temperature with time in a given shell is given by

$$\frac{dT_{\text{K}}}{dt} = -2HT_{\text{K}} + \frac{T_{\text{K}}}{\mu} \frac{d\mu}{dt} + \frac{2\mu m_{\text{p}}}{3k\rho_{\text{b}}} (\mathcal{H} - \Lambda), \quad (14)$$

where the photoionization heating rate is given by

$$\begin{aligned} \mathcal{H} &= \frac{1}{4\pi r^2} \left(\int_{I_{\text{HI}}}^{\infty} \frac{L_E e^{-\tau(r,E)}}{E} (E - I_{\text{HI}}) n_{\text{HI}} \sigma_{\text{HI}} f_{\text{heat}}(E, I_{\text{HI}}) dE \right. \\ &\quad + \int_{I_{\text{HeI}}}^{\infty} \frac{L_E e^{-\tau(r,E)}}{E} (E - I_{\text{HeI}}) n_{\text{HeI}} \sigma_{\text{HeI}} f_{\text{heat}}(E, I_{\text{HeI}}) dE \\ &\quad \left. + \int_{I_{\text{HeII}}}^{\infty} \frac{L_E e^{-\tau(r,E)}}{E} (E - I_{\text{HeII}}) n_{\text{HeII}} \sigma_{\text{HeII}} f_{\text{heat}}(E, I_{\text{HeII}}) dE \right), \end{aligned} \quad (15)$$

with $H(z)$ being the Hubble constant, ρ_{b} the average baryonic density of the Universe, μ the mean molecular weight and f_{heat} the fraction of the photoelectron energy that goes into gas heating, which depends on the photoelectron energy as given by Furlanetto & Stoever (2010).

The term proportional to Λ in equation (14) accounts for the radiative losses arising from collisional and recombination processes (the corresponding rates were adopted from Theuns et al. 1998), as well as for Compton cooling caused by scattering of the CMB on free electrons³, which proceeds on the time scale

$$\begin{aligned} t_{\text{CMB}} &= \frac{3m_e c^2 (n/n_e)}{32\sigma_{\text{T}}\sigma_{\text{CMB}}^4(z)} \\ &\approx 8 \times 10^7 \left(\frac{n_e}{n}\right)^{-1} \left(\frac{1+z}{11}\right)^{-4} \text{ yr}, \end{aligned} \quad (16)$$

where n is the total particle number density, σ_{T} is the Thomson scattering cross-section and σ is the Stefan–Boltzmann constant, cooling due to collisional processes (including bremsstrahlung) and CMB scattering proves to be important in the vicinity of the miniquasar where the gas becomes strongly ionized and its temperature rises to $T_{\text{K}} \gtrsim 10^4$ K. However, the cooling processes typically have a negligible effect on the average parameters of the IGM heating zone produced by the miniquasar.

We further assume that the spin temperature, T_{s} , characterizing the 21 cm transition is everywhere equal to the gas

³ Inverse Compton heating due to the X-ray radiation is negligible except very close to the miniquasar.

kinetic temperature, T_K . The EDGES measurement (Bowman et al. 2018) suggests that it is indeed the case at $z \lesssim 20$, implying that by that time the first stars had already created a significant UV (10.2–13.6 eV) background for decoupling the spin temperature from that of the CMB and bringing it close to the gas kinetic temperature via the Wouthuysen–Field effect (Wouthuysen 1952; Field 1958). Furthermore, the photoionization of the IGM by soft X-rays from a miniquasar will be accompanied by the creation of Ly α photons that will further strengthen the Wouthuysen–Field effect wherever the gas temperature increases by $\gtrsim 10^3 H(z)t_S \gtrsim 100$ K on the BH growth timescale (Chuzhoy, Alvarez, & Shapiro 2006; Chen & Miralda-Escudé 2008). Under these assumptions and for the adopted cosmological parameters, the brightness temperature of the 21 cm line is expected to be

$$T_b = 29 x_{\text{HI}} \left(\frac{1+z}{11} \right)^{1/2} \left(1 - \frac{1+z}{11} \frac{30}{T_K} \right) \text{mK}. \quad (17)$$

5 RESULTS

Our model has the following parameters: the initial and final redshifts (z_i and z_f), the initial and final masses of the BH (m_i and m_f , in solar masses), the Eddington ratio during active accretion phases (\dot{m}), and the intragalactic absorption column density and metallicity (N_{H} and Z , respectively). We now present a summary of results obtained for various sets of the parameter values. Most of the results presented below have been obtained for the case of purely thermal accretion disk emission, with the spectral shape as shown in the top panel of Fig. 1. We specify explicitly whenever we also take the possible contribution of a high-energy Comptonization component into account.

5.1 Gas temperature and 21 cm brightness temperature radial profiles

Figure 2 shows the IGM temperature and hydrogen ionization fraction as functions of comoving distance from the miniquasar and the brightness temperature of the resulting 21 cm signal as a function of the angular distance in the plane of the sky for $z_i = 15$, $z_f = 10$, $m_i = 2 \times 10^3$, $m_f = 10^4$, $\dot{m} = 1$ (the corresponding accretion duty cycle $k_{\text{duty}} = 40\%$) and various absorption characteristics: $Z = 0$, $N_{\text{H}} = 10^{18}$, 10^{20} , 10^{21} , 10^{22} cm^{-2} and $Z = 1$, $N_{\text{H}} = 10^{21}$. We see that the absorption of soft X-rays within the host galaxy leads to less efficient IGM heating if $N_{\text{H}} \gtrsim 10^{20} \text{ cm}^{-2}$ and that the presence of heavy elements ($Z = 1$ vs. $Z = 0$) proves to be of minor importance. Therefore, we hereafter focus on the metal-free case, unless specifically noted otherwise.

Figure 3 is analogous to Fig. 2, but the BH mass has been increased by an order of magnitude from $m_i = 2 \times 10^3$, $m_f = 10^4$ to $m_i = 2 \times 10^4$, $m_f = 10^5$. We see that the influence of intragalactic absorption is similar to the previous case and that the IGM heating zone has somewhat spread outwards.

Figure 4 demonstrates the dependence of the results on the BH mass. Here, we adopted $z_i = 15$, $z_f = 10$, $\dot{m} = 1$ and $N_{\text{H}} = 10^{20}$ and sampled BH masses (m_i , m_f) from $(2 \times 10^2, 10^3)$ to $(2 \times 10^5, 10^6)$. We see that although more massive BHs produce much stronger ionization very close to the source, this has a fairly small effect on the resulting 21 cm signal,

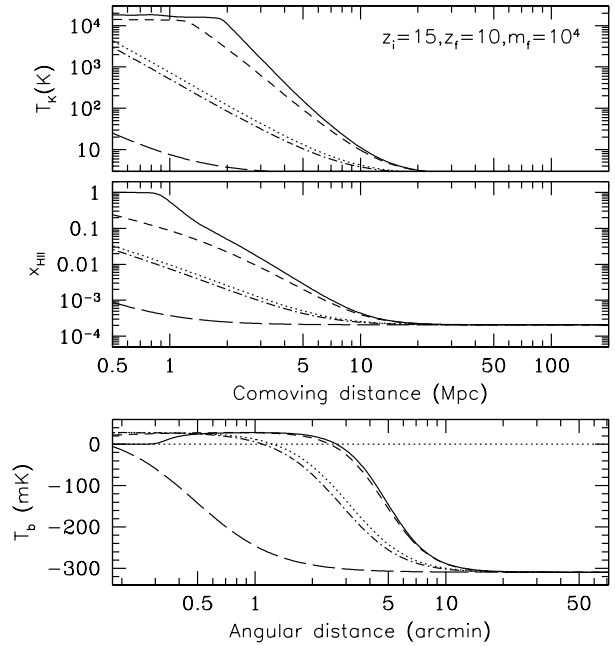


Figure 2. *Top panel:* IGM temperature as a function of comoving distance from the miniquasar for $z_i = 15$, $z_f = 10$, $m_i = 2 \times 10^3$, $m_f = 10^4$, $\dot{m} = 1$ and various parameters of intragalactic absorption [N_{H} (cm^{-2}), Z]: (10^{18} , 0) – solid, (10^{20} , 0) – short-dashed, (10^{21} , 0) – dotted, (10^{22} , 0) – long-dashed and (10^{21} , 1) – dash-dotted. *Middle panel:* hydrogen ionization fraction. *Bottom panel:* 21 cm brightness temperature as a function of angular distance from the miniquasar. These plots correspond to z_f .

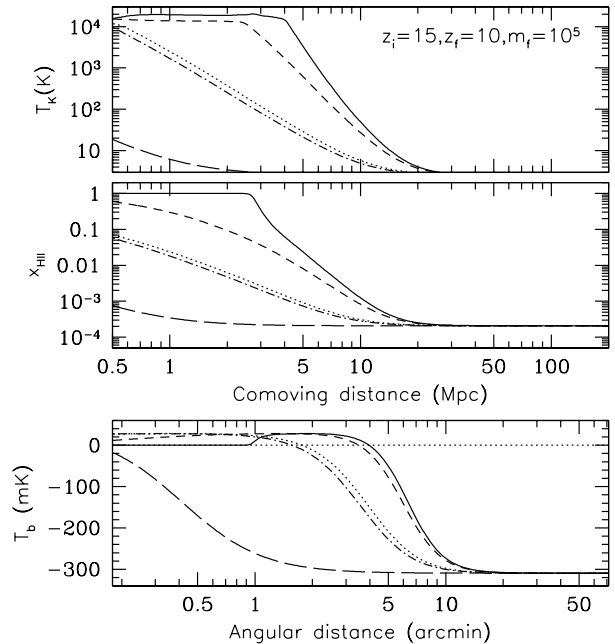


Figure 3. As Fig. 2, but for $m_i = 2 \times 10^4$ and $m_f = 10^5$.

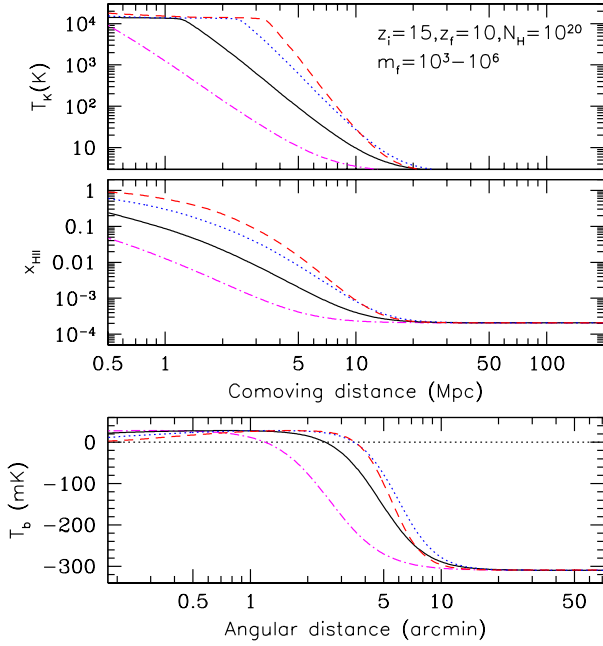


Figure 4. Similar to Fig. 2, but for a fixed absorption column ($N_{\text{H}} = 10^{20} \text{ cm}^{-2}$) and various BH masses (m_i, m_f): ($2 \times 10^2, 10^3$) – dash-dotted magenta, ($2 \times 10^3, 10^4$) – solid black, ($2 \times 10^4, 10^5$) – dotted blue, ($2 \times 10^5, 10^6$) – dashed red.

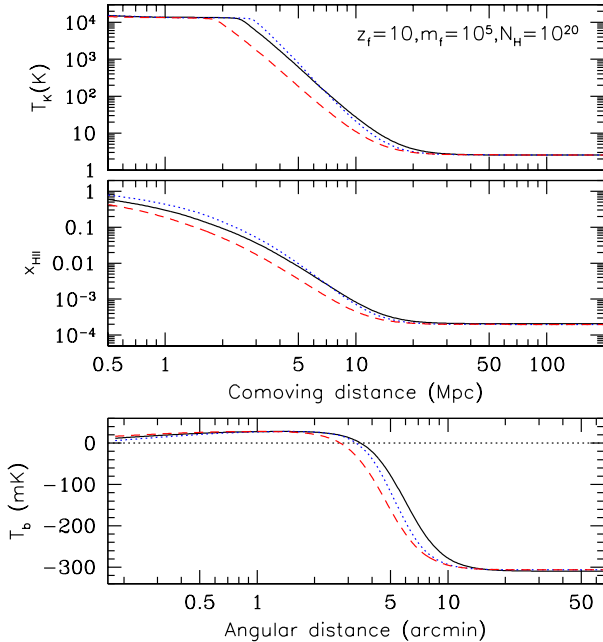


Figure 5. Similar to Fig. 2, but for fixed BH mass ($m_i = 2 \times 10^4, m_f = 10^5$) and absorption column ($N_{\text{H}} = 10^{20} \text{ cm}^{-2}$) and various scenarios of BH growth (z_i, z_f, \dot{m}): (15, 10, 1) – solid black, (20, 10, 1) – dotted blue, (20, 10, 0.5) – dashed red.

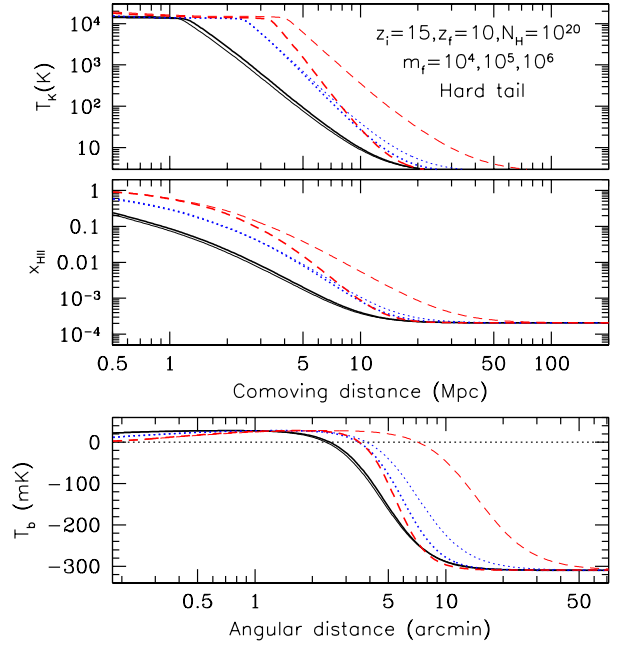


Figure 6. Similar to Fig. 2, for a fixed absorption column ($N_{\text{H}} = 10^{20} \text{ cm}^{-2}, Z = 0$), three sets of BH masses ($m_i = 2 \times 10^3, m_f = 10^4$ – solid black, $m_i = 2 \times 10^4, m_f = 10^5$ – dotted blue, $m_i = 2 \times 10^5, m_f = 10^6$ – dashed red) and two spectral models: pure thermal disk emission (*diskbb* – thick lines) and thermal disk emission with a Comptonization tail (*simpl*diskbb* – thin lines).

because the innermost region of strong heating is characterized by a nearly saturated, positive 21 cm brightness temperature [because $T_{\text{K}} \gg T_{\text{CMB}}$, see eq. (17)]. More important from an observational point of view is what happens at larger distances where the 21 cm signal changes from emission to absorption, and we see that the effective size of this region first noticeably increases on going from $m_f = 10^3$ to $m_f = 10^4$ and then remains nearly the same for $m_f = 10^5$ and $m_f \leq 10^6$ (in fact, this region is somewhat smaller for $m_f \leq 10^6$ than for $m_f = 10^5$ because of the smaller number of soft X-ray photons with $E \gtrsim 300 \text{ eV}$, capable of propagating to large distances, in the former case – see Fig. 1). This behavior is broadly consistent with the prediction made in §3 that the 21 cm zones around miniquasars should be largely determined by the total accretion energy for BHs with $M \lesssim 10^4 M_{\odot}$ and by the characteristic mean free path of accretion disk photons for more massive BHs.

Figure 5 demonstrates the influence of a particular history of BH growth on the results. Here, we fixed the final redshift at $z_f = 10$, the initial and final BH masses at $m_i = 2 \times 10^4$ and 10^5 , respectively, and the absorption column at $N_{\text{H}} = 10^{20}$, and considered three scenarios: (i) $z_i = 15, \dot{m} = 1$ (the duty cycle $k_{\text{duty}} = 40\%$), (ii) $z_i = 20, \dot{m} = 1$ ($k_{\text{duty}} = 27\%$) and (iii) $z_i = 20, \dot{m} = 0.5$ ($k_{\text{duty}} = 55\%$). We see that the differences in the corresponding T_{K} and T_{b} profiles are small.

So far we have assumed that the incident radiation spectrum is that of a multicolor accretion disk modified by line-of-sight absorption, as shown in the top panel of Fig. 1. We now wish to investigate the possible effect of an additional hard, power-law spectral component that may arise due to

the Comptonization of soft photons from the BH accretion disk in its hot corona. To this end, we carried out calculations for our *simpl*diskbb* spectral models for $m_f = 10^4$, 10^5 and 10^6 and $N_H = 10^{20} \text{ cm}^{-2}$, shown in the bottom panel of Fig. 1. The resulting T_K , x_{HII} and T_b radial profiles are compared in Fig. 6 with those computed without the hard X-ray component. We see that the 21 cm zone is almost unaffected by the hard spectral component for the least massive BH ($m_f = 10^4$), somewhat broadens in the intermediate mass case ($m = 10^5$), and becomes substantially (by a factor of ~ 2) larger for the heaviest BH ($m = 10^6$). The last result is unsurprising, because the corresponding X-ray spectrum (see Fig. 1) is dominated by the power-law component already at $E \sim 300 \text{ eV}$ (partially because of the adopted substantial line-of-sight absorption of 10^{20} cm^{-2}).

5.2 Characteristic size of the 21 cm zone

From the above comparison of the computed T_b radial profiles a preliminary conclusion may be drawn that the spatial extent of the 21 cm signal associated with a high-redshift miniquasar will only weakly depend on the properties of the latter. For more quantitative assessment, we define two characteristic angular sizes: θ_0 – the projected distance from the miniquasar at which the 21 cm signal changes from emission to absorption, i.e. $T_b(\theta_0) = 0$, and $\theta_{1/2}$ – the radius at which the brightness temperature of the absorption signal is half the ‘background’ value (the 21 cm brightness temperature outside of the miniquasar heating zone), i.e. $T_b(\theta_{1/2}) = T_{b,\text{bgr}}/2$. Under our assumptions that there is no global IGM heating and that the 21 cm spin temperature is coupled to the IGM kinetic temperature, $T_{b,\text{bgr}} = -245 \text{ mK}$ and -307 mK at $z_f = 15$ and $z_f = 10$, respectively.

Figure 7 (top panel) shows θ_0 and $\theta_{1/2}$ as functions of the absorption column for $z_i = 15$, $z_f = 10$, $\dot{m} = 1$ and three different BH masses, $m_f = 10^4$, 10^5 and 10^6 . We see that if the intragalactic absorption is not strong ($N_H \lesssim 10^{20} \text{ cm}^{-2}$), θ_0 and especially $\theta_{1/2}$ depend only weakly on the BH mass and absorption column density. Specifically, $\theta_0 \sim 2.5\text{--}5 \text{ arcmin}$, and $\theta_{1/2} \sim 5\text{--}7 \text{ arcmin}$. If $N_H \gtrsim 10^{21} \text{ cm}^{-2}$, most of the microquasar’s soft X-ray emission is absorbed within its host galaxy, which naturally leads to a dramatic weakening of IGM heating and shrinkage of the 21 cm zone. The bottom panel of Fig. 7 shows a similar set of curves for the case of miniquasars operating at higher redshifts, namely $z_i = 20$ and $z_f = 15$. In this case, there is a more noticeable, albeit still weak dependence on the BH mass, namely (for $N_H \lesssim 10^{20} \text{ cm}^{-2}$) θ_0 changes from ~ 1.5 to $\sim 3 \text{ arcmin}$ as m_f increases from 10^4 to 10^6 , whereas $\theta_{1/2}$ changes from ~ 2.5 to $\sim 4.5 \text{ arcmin}$ in the same BH mass range. Overall, the computed θ_0 size of the heating zone is in remarkably good agreement (within a factor of ~ 2) with our rough prediction given by equation (8).

Figure 8 demonstrates the impact of an additional hard (Comptonization) spectral component on the extent of the miniquasar 21 cm zone. By comparing these plots with those pertaining to the case of pure multicolor disk emission (Fig. 7), we see that while θ_0 and $\theta_{1/2}$ have remained nearly unchanged for $m_f \leq 10^5$, these characteristic radii have increased by a factor of $\sim 1.5\text{--}2$ for $m_f = 10^6$. Therefore, the hard tail considerably changes the overall picture for the most massive of the considered BHs ($m = 10^6$). This again

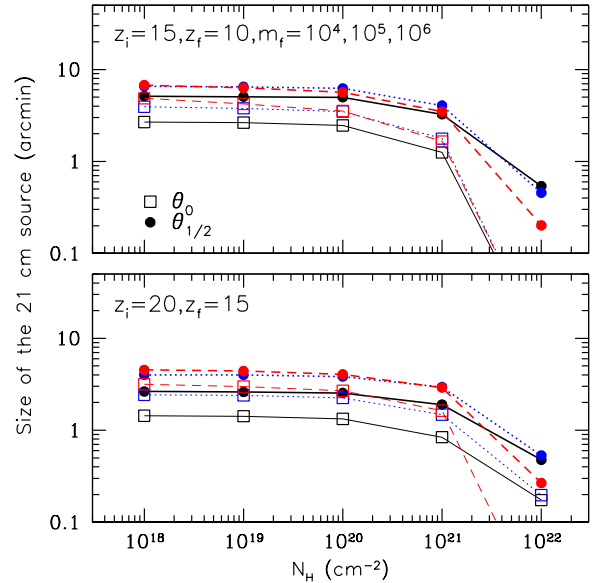


Figure 7. *Top panel:* Characteristic angular sizes (see text for definitions) θ_0 (empty squares connected by thin lines) and $\theta_{1/2}$ (filled circles connected by thick lines) of the 21 cm signal around a miniquasar as a function of the absorption column for $z_i = 15$, $z_f = 10$, $\dot{m} = 1$ and three sets of BH masses (m_i, m_f): ($2 \times 10^3, 10^4$) – solid black, ($2 \times 10^4, 10^5$) – dotted blue, and ($2 \times 10^5, 10^6$) – dashed red. *Bottom panel:* Similar, for $z_i = 20$ and $z_f = 15$.

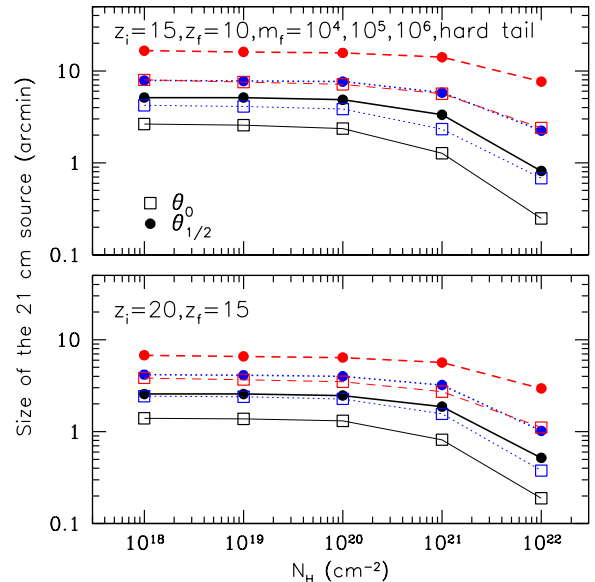


Figure 8. As Fig. 7, but for thermal disk emission with a Comptonization tail (*simpl*diskbb*) instead of pure thermal disk emission.

reflects the fact that, within the adopted model, the Comptonized radiation starts to dominate over the thermal emission already at photon energies ~ 300 eV.

5.3 Spectrum and flux of the 21 cm signal

We now proceed to discussing the spectral properties of the 21 cm signal associated with high-redshift miniquasars. Based on the above results we can expect such objects to be surrounded on the sky by fairly well defined regions with an apparent size of several arcmin within which $T_b - T_{b,\text{bgr}} \gtrsim 100$ mK, and it will be interesting to search for such specific zones of 21 cm excess emission with future radio interferometers.

In reality, the effective angular size of the 21 cm signal extraction region around a candidate miniquasar will be determined by the characteristics of a particular radio interferometer and by the related noise and background levels (see the discussion in §7 below), but ideally it should be of the order of the $\theta_{1/2}$ radius defined above. We have therefore integrated the surface brightness of the expected 21 cm excess emission (i.e. the difference $T_b - T_{b,\text{bgr}}$) over the circle of radius $\theta_{1/2}$ around the miniquasar.

Figure 9 (top panel) shows the resulting spectra for $z_i = 15$, $z_f = 10$, $m_i = 2 \times 10^4$, $m_f = 10^5$, $\dot{m} = 1$ and various absorption columns. We see that the 21 cm flux density is almost unaffected by intragalactic absorption if $N_{\text{H}} \lesssim 10^{20} \text{ cm}^{-2}$, the signal weakens by a factor of ~ 3 for $N_{\text{H}} = 10^{21} \text{ cm}^{-2}$ and nearly vanishes if $N_{\text{H}} = 10^{22} \text{ cm}^{-2}$, as essentially no soft X-rays from the miniquasar leak from the host galaxy into the IGM.

The middle panel of Fig. 9 demonstrates the dependence of the 21 cm spectrum on the BH mass (for $z_i = 15$, $z_f = 10$, $\dot{m} = 1$ and $N_{\text{H}} = 10^{20} \text{ cm}^{-2}$). We see that the signal increases by a factor of ~ 3 on going from $m_f = 10^3$ to 10^4 and then remains nearly the same (within a factor of ~ 1.5) for $m_f = 10^4 - 10^6$. The bottom panel of Fig. 9 shows the corresponding spectra for similar miniquasars at higher redshifts: $z_i = 20$, $z_f = 15$. The picture is qualitatively similar to the previous case, but the 21 cm excess flux density is more sensitive to the BH mass at the higher redshift. We also note that the signal is somewhat stronger for $m_f = 10^5$ than for $m_f = 10^6$ in the $z_f = 10$ case, while the opposite is true for $z_f = 15$. The reason is that this signal is accumulated from the $\theta_{1/2}$ region whose dependence on the BH mass (see Fig. 7) is slightly different between $z_f = 10$ and $z_f = 15$ due to a non-trivial interplay between the BH soft X-ray spectral properties and redshift-dependent density of the IGM. Most importantly, however, Fig. 9 demonstrates that the expected 21 cm signal depends fairly weakly (within a factor of 3) on the BH mass over the $10^4 - 10^6 M_\odot$ range.

Figure 10 demonstrates the impact of an additional hard spectral component on the discussed 21 cm spectra. We see that the hard tail leads to a dramatic increase of the expected 21 cm signal for our most massive ($m_f = 10^6$) BH, with this difference being more pronounced at the lower redshift ($z_f = 10$ vs. $z_f = 15$). These tendencies are expected, since the reported spectra were obtained by integration of T_b within the characteristic radius $\theta_{1/2}$, which increases in the presence of a hard spectral component, as was shown in §5.2.

As regards the absolute value of the expected 21 cm flux

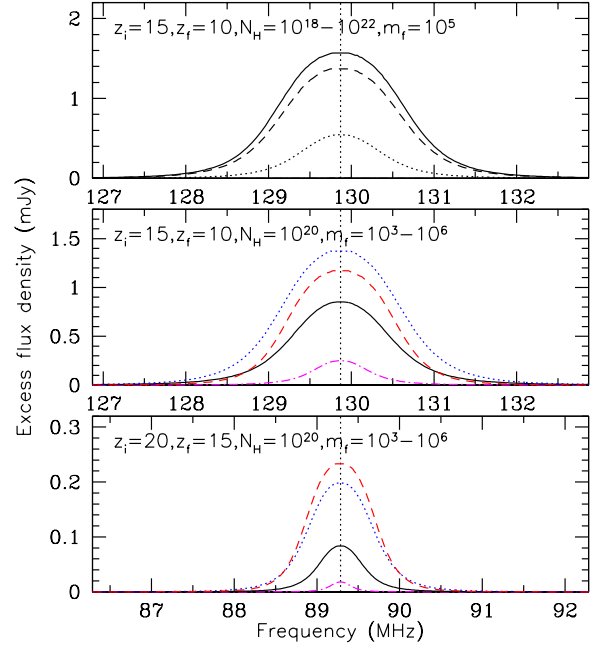


Figure 9. *Top panel:* Spectra of 21 cm excess emission (with respect to the background level at the miniquasar’s redshift) integrated within $\theta_{1/2}$ for $z_i = 15$, $z_f = 10$, $\dot{m} = 1$, $m_i = 2 \times 10^4$, $m_f = 10^5$ and various N_{H} columns (cm^{-2}): 10^{18} (solid), 10^{20} (dashed), 10^{21} (dotted), 10^{22} (dash-dotted, poorly visible near the lower boundary of the plot). *Middle panel:* Similar, for a fixed absorption column ($N_{\text{H}} = 10^{20} \text{ cm}^{-2}$) and various BH masses (m_i , m_f): (2×10^4 , 10^3) – dash-dotted magenta, (2×10^3 , 10^4) – solid black, (2×10^4 , 10^5) – dotted blue, and (2×10^5 , 10^6) – dashed red. *Bottom panel:* Similar, for higher redshifts, $z_i = 20$, $z_f = 15$.

density, it is useful to approximate it as follows:

$$F_\nu \approx \frac{2k}{(21 \text{ cm})^2 (1+z)^2} \frac{3|T_{b,\text{bgr}}|}{4} \pi \theta_{1/2}^2, \\ \approx 0.6 \left(\frac{1+z_f}{11} \right)^{-2} \frac{|T_{b,\text{bgr}}|}{250 \text{ mK}} \left(\frac{\theta_{1/2}}{5'} \right)^2 \text{ mJy}, \quad (18)$$

where we assumed that the average excess brightness temperature of the 21 cm signal within $\theta_{1/2}$ is $3T_{b,\text{bgr}}/4$, which is approximately the case (see the T_b radial profiles in §5.1). Substituting the typical values derived from our simulations for $z_f = 10$ ($T_{b,\text{bgr}} = -309$ mK, $\theta_{1/2} = 6'$) and $z_f = 15$ ($T_{b,\text{bgr}} = -245$ mK, $\theta_{1/2} = 4'$) into the above expression, we find $F_\nu \approx 1.1$ and 0.18 mJy, respectively, in fairly good agreement with the 21 cm spectra shown above.

We finally note that the simulated 21 cm spectra for the case of purely thermal disk emission are characterized by FWHM of ≈ 0.01 in terms of $\Delta\nu/\nu$.

6 RELATION TO X-RAY OBSERVATIONS

As was discussed in §1, there is a hope that future X-ray observatories such as *Lynx* will be able to find a significant number of high-redshift miniquasar candidates. Provided that the planned next-generation radio facilities such as SKA are also available by that time, it should be possible to search for the specific 21 cm signatures of X-ray selected miniquasars discussed in this paper.

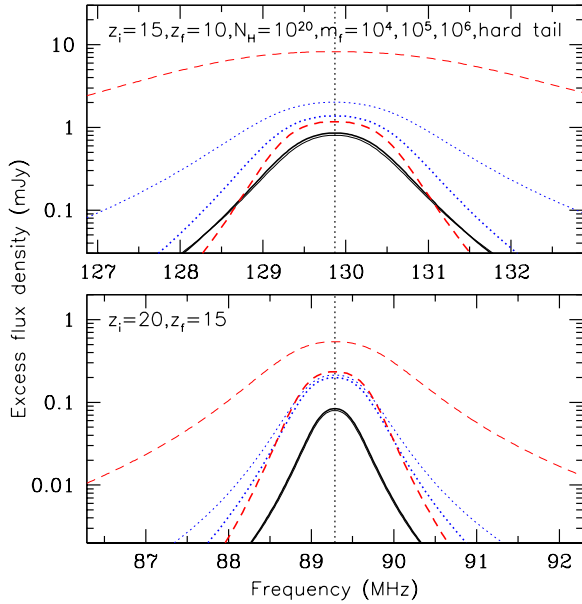


Figure 10. Similar to Fig. 9, comparing the case of pure thermal disk emission (*diskbb*, thick curves) with that of a combination of disk emission and a Comptonization tail (*simpl*diskbb*, thin curves), for three sets of BH masses (m_i, m_f): $(2 \times 10^3, 10^4)$ – solid black, $(2 \times 10^4, 10^5)$ – dotted blue and $(2 \times 10^5, 10^6)$ – dashed red. Note the logarithmic vertical scale.

The first practical question then is: what are the limiting BH mass and redshift for X-ray detection of miniquasars? In this study, we have assumed that a miniquasar’s spectrum is a combination of (i) multicolor disk emission with the temperature expected from the standard accretion disk theory and, plausibly, (ii) a hard, power-law ($\Gamma \approx 2$) tail associated with Comptonization of disk emission in a hot corona, which extends to high energies (at least to a few tens of keV). It is this additional hard component that an X-ray telescope might be able to detect from a high-redshift miniquasar. In the particular spectral model, *simpl(diskbb)*, used in this study, the observed X-ray flux in the 0.5–2 keV band (corresponding to emission in a rest-frame band of $0.5(1+z)$ – $2(1+z)$ keV), F_X , is proportional to the fraction of scattered photons. It turns out that, virtually independently of the BH mass and accretion rate,

$$F_X \approx 0.06 \frac{f_{sc}}{0.05} \frac{L}{4\pi D_L^2}, \quad (19)$$

where L is the total luminosity of the miniquasar and $D_L(z)$ is its luminosity distance.

Assuming that $f_{sc} = 0.05$ (which is a reasonable value as discussed in §2.2) and that the X-ray telescope catches the miniquasar when it is accreting at a critical rate ($\dot{m} = 1$), when $L = L_{Edd}(m)$, we find from equation (19) that for $m = 10^4$, $F_X = 2.3 \times 10^{-20}$ and 5.8×10^{-20} erg cm $^{-2}$ s $^{-1}$ at $z = 15$ and $z = 10$, respectively, whereas for $m = 10^5$, $F_X = 2.3 \times 10^{-19}$ and 5.8×10^{-19} erg cm $^{-2}$ s $^{-1}$ for the same redshifts. These fluxes are well below the detection threshold of *Chandra*, the most sensitive X-ray telescope so far. However, the proposed *Lynx* mission is expected to reach a sensitivity of

$\sim 10^{-19}$ erg cm $^{-2}$ s $^{-1}$ in its deep extragalactic surveys and should thus be able to detect actively growing BHs of mass $\gtrsim 5 \times 10^4 M_\odot$ at $z = 15$ and $\gtrsim 2 \times 10^4 M_\odot$ at $z = 10$. These mass limits are of course inversely proportional to \dot{m} and f_{sc} .

7 DISCUSSION AND SUMMARY

We have shown that an intermediate mass BH growing by radiatively efficient accretion in the early Universe should leave a specific, localized imprint on the 21 cm cosmological signal. Namely, a miniquasar with the BH mass between $\sim 10^4$ and $\sim 10^6 M_\odot$ at $z \sim 15$ – 10 will be surrounded by a region with a fairly well defined boundary of several arcmin radius, within which the 21 cm temperature quickly grows inwards from the background value $T_{b,bgr} \sim -250$ mK to $T_b \sim 0$ (reaching the saturation value of ~ 30 mK in the innermost region). The size of this region and the flux density of the enclosed 21 cm signal are only weakly sensitive to the BH mass in the range quoted above.

7.1 Sensitivity to assumptions

The above result was obtained under certain assumptions and it is important to discuss how realistic they are. Perhaps, the most important constituent of our model is the miniquasar’s spectral energy distribution, which we assumed to be that of multicolor disk blackbody emission. As was discussed in §2.1, the actual spectrum of the accretion disk emission is likely to deviate significantly from this simplistic model, but given the weak sensitivity of the size of the 21 cm zone to the BH mass, such deviations are unlikely to have a significant effect on our predictions. More important is the likely presence of an additional, hard component in the miniquasar spectrum. As we have demonstrated, its effect is small for relatively low-mass BHs ($\sim 10^4$ – $10^5 M_\odot$) but becomes substantial (the heating zone widens by a factor of ~ 1.5 – 2) for a $10^6 M_\odot$ BH.

The next important issue is possible photoabsorption of the miniquasar’s soft X-ray emission within its host galaxy. It turns out that the properties of the 21 cm zone remain nearly unchanged as long as $N_H \lesssim 10^{20}$ cm $^{-2}$ (regardless of the presence of metals in the absorbing medium), but at $N_H \sim 10^{21}$ cm $^{-2}$ this zone starts to shrink dramatically. One may argue that a powerful miniquasar should be able to quickly photoionize the interstellar medium within a substantial distance of itself and thus effectively reduce N_H (e.g. Sazonov & Khabibullin 2018), but this clearly needs further investigation. Furthermore, if miniquasars are less powerful analogs of AGN, they may have a small-scale obscuring torus of cold gas and dust. In that case there will be two opposite cones of specific 21 cm signal around the miniquasar, i.e. the average signal within the $\theta_{1/2}$ radius will decrease by a factor of $\Omega/4\pi$, where Ω is the solid angle of the unobscured sky as seen from the BH.

Finally, we assumed that the Universe had not yet been globally heated at the redshifts of interest ($z \sim 15$ – 10) and that the 21 cm spin temperature was coupled to the gas temperature at these epochs. It is only in this case that a large contrast in the 21 cm brightness temperature will arise between the vicinity of the miniquasar, where $T_b \sim 0$, and the background, where $T_b \sim -(200$ – $300)$ mK (at $z = 15$ – 10).

These assumed conditions are in good agreement with the recent EDGES result (Bowman et al. 2018) for $z \sim 20\text{--}15^4$ but appear to fail at $z \lesssim 14$, when the global 21 cm temperature has been measured to be around zero. Of course, the EDGES measurements must be verified with future observations but a lot of authors (see §1) have suggested that XRBs, miniquasars and other types of X-ray sources can indeed significantly heat the Universe by $z \sim 10$. In such a case, it will be extremely difficult to discern the 21 cm imprint of an individual miniquasar against the background at $z \sim 10$ but that should still be possible at $z \sim 15$.

7.2 Comparison with previous studies

The present study is not the first one addressing the potential impact of high-redshift X-ray sources on the cosmological 21 cm signal. In particular, a number of authors have focused on the expected 21 cm signatures of individual quasars and miniquasars in the early Universe (Chuzhoy, Alvarez, & Shapiro 2006; Thomas & Zaroubi 2008; Yajima & Li 2014; Ghara et al. 2017; Bolgar et al. 2018; Vasiliev, Sethi, & Shchekinov 2018). The crucial novel aspect of our study is its focus on the (relatively soft) thermal emission of the accretion disk around an intermediate-mass black hole, which is expected (based on the rich observational material on high Eddington ratio X-ray binaries and AGN) to carry the bulk of the bolometric luminosity of the miniquasar but has been usually ignored before. This leads to an important difference for the predicted 21 cm signature, namely that it should be concentrated within ~ 5 arcmin of the miniquasar due to the relatively short mean free path of the extreme UV/soft X-ray photons in the ambient IGM.

Furthermore, in contrast to some of the previous studies we have assumed the 21 cm spin temperature at the considered epochs ($z \sim 15\text{--}10$) to be coupled (by the UV background from the first stars) to the gas temperature throughout the IGM and that the latter had not yet been heated significantly on average, so that the mean $T_b \sim -(200\text{--}300)$ mK, rather than $T_b \approx 0$ as it would be in the absence of Wouthuysen–Field coupling or in the presence of significant global heating. This key assumption, as noted above (in §7.1), is partially motivated by the recent detection of a strong 21 cm global absorption feature by EDGES. It is the combination of the relative compactness of the heating zone and the large negative global 21 cm brightness temperature that has led to our conclusion that high-redshift miniquasars might be associated with fairly strong ($\sim 0.2[(1+z)/16]^{-2}$ mJy) 21 cm signatures.

7.3 Observational strategy

A blind sky search for weak 21 cm signals from individual high-redshift miniquasars might not be feasible in the near future. Therefore, we propose to look for such signals specifically from miniquasar candidates that can be found with the proposed *Lynx* X-ray mission. As discussed in §6, the planned *Lynx* sensitivity of $\sim 10^{-19}$ erg cm $^{-2}$ s $^{-1}$ should allow it to detect rapidly growing BHs with masses as low as a

few $10^4 M_\odot$ out to $z \sim 15$, provided that a significant fraction of the energy released by accretion goes into Comptonized, hard X-ray radiation.

However, selection of such candidates is unlikely to be an easy task. Indeed, *Lynx* will provide only crude X-ray hardness information for them, not sufficient for distinguishing from other types of sources. Moreover, high-redshift miniquasars will probably be just a small minority among the tens of thousands of sources to be detected in the proposed *Lynx* (400 arcmin 2) ultradeep survey (The Lynx Team 2018). Specifically, Ben-Ami, Vikhlinin, & Loeb (2018) predict that between several dozen and a few thousand growing massive BHs (roughly in the $10^4\text{--}10^6 M_\odot$ range of interest to us) could be found at $z \sim 5\text{--}12$, with this large uncertainty reflecting our poor understanding of how BHs form and grow in the early Universe. In the present study, we have focused on somewhat earlier epochs, $z \sim 15\text{--}10$, and just between a few and a few hundred (i.e. less or much less than 1 object per arcmin 2) such high-redshift miniquasars are expected to be found by *Lynx* (Ben-Ami, Vikhlinin, & Loeb 2018).

Fortunately, there are bright prospects for the synergy between the proposed *Lynx* survey and the optical/IR ultradeep surveys by next-generation telescopes such as *JWST* (The Lynx Team 2018), so that the majority of the *Lynx* sources (such as AGN and galaxies) will probably have reliable optical/IR counterparts. High-redshift miniquasars, because of their expected optical/IR faintness (see §1), will thus be hidden among the relatively small sample of very faint ($F_X \gtrsim 10^{-19}$ erg cm $^{-2}$ s $^{-1}$) X-ray sources *without* an optical counterpart. A reasonable approach would then be to regard all such sources as candidate high-redshift miniquasars and search for specific 21-cm signatures around their positions provided by *Lynx*.

According to our estimates, high-redshift miniquasars are expected to produce 21 cm signals with an amplitude ~ 100 mK on few-arcmin scales, with the characteristic spectral width $\Delta\nu/\nu \sim 0.01$ corresponding to $\Delta\nu \sim 1$ MHz at $\nu \sim 100$ MHz for $z = 10\text{--}15$. How do these numbers compare with the expected characteristics of future cosmological 21 cm surveys with their specific noise levels and angular resolution? Figure 11 shows the result of convolution of our predicted 21 cm images of miniquasars (for $m = 10^4\text{--}10^6$ and $z_f = 10$ and 15) with two-dimensional Gaussians with $\sigma = 5'$ and $10'$. We see that miniquasars are expected to produce $\sim 140\text{--}180$ mK and $\sim 50\text{--}80$ mK positive peaks (with respect to the large-scale background) on images with 5-arcmin angular resolution for $z \sim 10$ and $z \sim 15$, respectively.

The low-frequency component of the SKA experiment, SKA-low, is planned to cover a broad frequency range extending down to ~ 50 MHz (allowing one to probe the early Universe out to $z \sim 25$) with high spectral resolution (~ 1 kHz) and a very large collecting area ~ 1 km 2 (Mellema et al. 2013). For the first phase of the experiment (the so-called SKA1-Low), the noise level is expected to be ~ 3 mK (~ 10 mK) for $z = 10$ ($z = 15$) images with $5'$ angular resolution (with the frequency bandwidth matched to the angular resolution) accumulated over an integration time of ~ 1000 hours (see fig. 2 in Mellema et al. 2015). Therefore, the ~ 100 mK signal from a high-redshift miniquasar (see Fig. 11) should be reliably detectable with such long (but feasible) observations by SKA1-low (and even more so by the fully constructed SKA-low).

⁴ Actually, EDGES measured an even lower sky-averaged $T_b \sim -500$ mK.

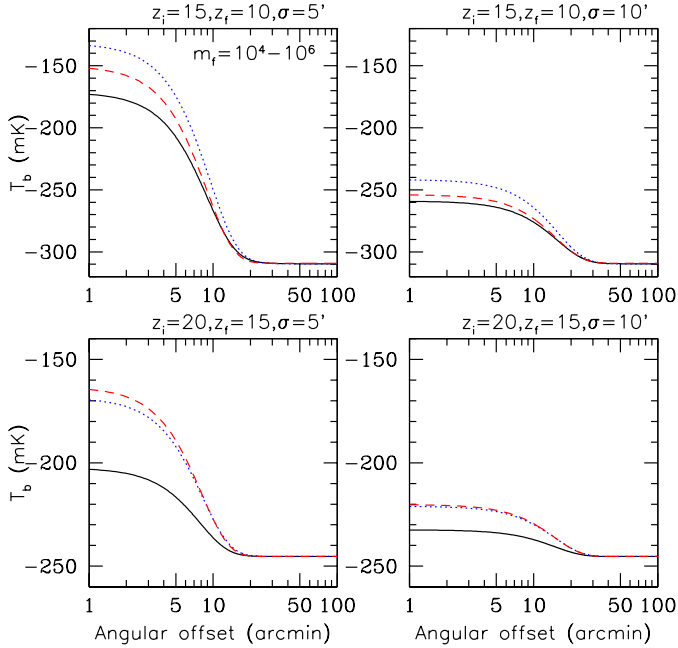


Figure 11. Radial profiles of the 21 cm images of miniquasars after convolution with a 2-dimensional Gaussian with $\sigma = 5'$ (left) and $10'$ (right). The upper panels are for $z_i = 15$ and $z_f = 10$, and the lower ones for $z_i = 20$ and $z_f = 15$. The different curves correspond to different BH masses (m_i, m_f): ($2 \times 10^3, 10^4$) – solid black, ($2 \times 10^4, 10^5$) – dotted blue, ($2 \times 10^5, 10^6$) – dashed red. These results are for multicolor disk emission and $N_H = 10^{20} \text{ cm}^{-2}$. Note the logarithmic horizontal scale.

In reality, the biggest problem will likely be separating the 21 cm signal associated with high-redshift miniquasars from astrophysical foregrounds of much higher amplitude, such as Galactic synchrotron radiation and cumulative emission from unresolved extragalactic sources; furthermore, the large-scale structure of the early Universe will cause additional fluctuations of the 21 cm brightness temperature on the arcmin scales relevant to the problem in hand (see [Mellema et al. 2013](#) for a review). Finally, as with any radio interferometer, SKA will not be capable of measuring absolute source fluxes due to the zero-spacing problem. A thorough consideration of these non-trivial observational issues is beyond the scope of this proof-of-concept study, but a number of recent studies ([Wyithe, Geil & Kim 2015](#); [Ghara et al. 2017](#)) address these problems in the context of SKA and suggest that there are efficient methods of evaluation and subtraction of foregrounds that might enable detection of the ~ 100 mK peaks associated with high-redshift miniquasars on the SKA images.

We finally emphasize again that such a search will be greatly facilitated by the availability of accurate celestial coordinates of candidate miniquasars from *Lynx*, even though the X-ray data will not provide their redshifts. In practice, the search might consist of browsing SKA-low images constructed with $\sim 5'$ angular resolution (and cleaned as carefully as possible from the foregrounds), one redshift slice after another over a range of $z \sim 10$ – 20 . The detection of a positive ~ 100 mK peak (see Fig. 11) centered on the *Lynx* position will strongly indicate that the object is indeed an intermediate-mass BH growing to become a supermassive

BH. Moreover, its redshift can thus be measured to within $\Delta z/(1+z) \lesssim 0.01$.

ACKNOWLEDGMENTS

The authors thank the referee for useful suggestions. The research was supported by the Russian Science Foundation (grant 14-12-01315).

REFERENCES

- Arnaud K. A., 1996, *ASPC*, 101, 17
 Bañados E., et al., 2018, *Natur*, 553, 473
 Ben-Ami S., Vikhlinin A., Loeb A., 2018, *ApJ*, 854, 4
 Bolgar F., Eames E., Hottier C., Semelin B., 2018, *MNRAS*, 478, 5564
 Bowman J. D., Rogers A. E. E., Monsalve R. A., Mozdzen T. J., Mahesh N., 2018, *Natur*, 555, 67
 Chen X., Miralda-Escudé J., 2008, *ApJ*, 684, 18
 Chuzhoy L., Alvarez M. A., Shapiro P. R., 2006, *ApJ*, 648, L1
 Cohen A., Fialkov A., Barkana R., Lotem M., 2017, *MNRAS*, 472, 1915
 Davis S. W., Blaes O. M., Hubeny I., Turner N. J., 2005, *ApJ*, 621, 372
 Done C., Gierliński M., Kubota A., 2007, *A&ARv*, 15, 1
 Done C., Davis S. W., Jin C., Blaes O., Ward M., 2012, *MNRAS*, 420, 1848
 Elvis M., et al., 1994, *ApJS*, 95, 1
 Ferrara A., Loeb A., 2013, *MNRAS*, 431, 2826
 Fialkov A., Cohen A., Barkana R., Silk J., 2017, *MNRAS*, 464, 3498
 Field G. B., 1958, *PIRE*, 46, 240
 Fragos T., et al., 2013, *ApJ*, 764, 41
 Furlanetto S. R., Stoever S. J., 2010, *MNRAS*, 404, 1869
 Ghara R., Choudhury T. R., Datta K. K., Choudhuri S., 2017, *MNRAS*, 464, 2234
 Gilfanov M., Merloni A., 2014, *SSRv*, 183, 121
 Kaaret P., Feng H., Roberts T. P., 2017, *ARA&A*, 55, 303
 Koratkar A., Blaes O., 1999, *PASP*, 111, 1
 Latif M. A., Ferrara A., 2016, *PASA*, 33, e051
 Leite N., Evoli C., D’Angelo M., Ciardi B., Sigl G., Ferrara A., 2017, *MNRAS*, 469, 416
 The Lynx Team, 2018, arXiv, arXiv:1809.09642
 Madau P., Rees M. J., Volonteri M., Haardt F., Oh S. P., 2004, *ApJ*, 604, 484
 Madau P., Fragos T., 2017, *ApJ*, 840, 39
 Makishima K., Maejima Y., Mitsuda K., Bradt H. V., Remillard R. A., Tuohy I. R., Hoshi R., Nakagawa M., 1986, *ApJ*, 308, 635
 Mason C. A., Trenti M., Treu T., 2015, *ApJ*, 813, 21
 Mellema G., et al., 2013, *ExA*, 36, 235
 Mellema G., Koopmans L., Shukla H., Datta K. K., Mesinger A., Majumdar S., 2015, *aska.conf*, 10, *aska.conf*
 Merloni A., Fabian A. C., Ross R. R., 2000, *MNRAS*, 313, 193
 Mirabel I. F., Dijkstra M., Laurent P., Loeb A., Pritchard J. R., 2011, *A&A*, 528, A149
 Narayan R., Salřdowski A., Soria R., 2017, *MNRAS*, 469, 2997
 Planck Collaboration, et al., 2016, *A&A*, 594, A13
 Pritchard J. R., Furlanetto S. R., 2007, *MNRAS*, 376, 1680
 Pritchard J. R., Loeb A., 2012, *RPPh*, 75, 086901
 Ricotti M., Ostriker J. P., 2004, *MNRAS*, 352, 547
 Ross H. E., Dixon K. L., Iliev I. T., Mellema G., 2017, *MNRAS*, 468, 3785
 Sazonov S. Y., Ostriker J. P., Sunyaev R. A., 2004, *MNRAS*, 347, 144

- Sazonov S., Sunyaev R., 2015, MNRAS, 454, 3464
Sazonov S., Khabibullin I., 2017, Astron. Lett., 43, 243
Sazonov S., Khabibullin I., 2017, MNRAS, 468, 2249
Sazonov S., Khabibullin I., 2018, MNRAS, 476, 2530
Sazonov S. Y., Lutovinov A. A., Krivonos R. A., 2014, AstL, 40, 65
Seager S., Sasselov D. D., Scott D., 1999, ApJ, 523, L1
Shakura N. I., Sunyaev R. A., 1973, A&A, 24, 337
Steiner J. F., Narayan R., McClintock J. E., Ebisawa K., 2009, PASP, 121, 1279
Takeo E., Inayoshi K., Ohsuga K., Takahashi H. R., Mineshige S., 2019, arXiv, arXiv:1901.04514
Telfer R. C., Zheng W., Kriss G. A., Davidsen A. F., 2002, ApJ, 565, 773
Theuns T., Leonard A., Efstathiou G., Pearce F. R., Thomas P. A., 1998, MNRAS, 301, 478
Thomas R. M., Zaroubi S., 2008, MNRAS, 384, 1080
Vasiliev E. O., Sethi S. K., Shchekinov Y. A., 2018, ApJ, 865, 130
Verner D. A., Ferland G. J., Korista K. T., Yakovlev D. G., 1996, ApJ, 465, 487
Volonteri M., 2010, A&ARv, 18, 279
Woods T. E., et al., 2018, arXiv, arXiv:1810.12310
Wouthuysen S. A., 1952, AJ, 57, 31
Wyithe S., Geil P., Kim H., 2015, aska.conf, 15, aska.conf
Yajima H., Li Y., 2014, MNRAS, 445, 3674

This paper has been typeset from a $\text{\TeX}/\text{\LaTeX}$ file prepared by the author.